



Kelvin probe force microscopy of the nanoscale electrical surface potential barrier of metal/semiconductor interfaces in ambient atmosphere

Petr Knotek¹, Tomáš Plecháček², Jan Smolík¹, Petr Kutálek^{*2,§}, Filip Dvořák³, Milan Vlček⁴, Jiří Navrátil⁵ and Čestmír Drašar⁵

Full Research Paper

[Open Access](#)

Address:

¹University of Pardubice, Faculty of Chemical Technology, Department of General and Inorganic Chemistry, Studentská 573, 532 10 Pardubice, Czech Republic, ²University of Pardubice, Faculty of Chemical Technology, Joint Laboratory of Solid State Chemistry, Studentská 84, 532 10 Pardubice, Czech Republic, ³University of Pardubice, Faculty of Chemical Technology, Center of Materials and Nanotechnologies, Studentská 95, 532 10, Pardubice, Czech Republic, ⁴Institute of Macromolecular Chemistry of the Academy of Sciences of the Czech Republic v.v.i., Heyrovsky sq. 2, 12006 Prague, Czech Republic and ⁵University of Pardubice, Faculty of Chemical Technology, Institute of Applied Physics and Mathematics, Studentská 95, 532 10, Pardubice, Czech Republic

Email:

Petr Kutálek* - petr.kutalek@upce.cz

* Corresponding author

§ Tel.: +420 466036155; fax: +420 466036011

Keywords:

Kelvin probe atomic force microscope; nanoinclusion; Schottky barrier; thermoelectric materials; work function

Beilstein J. Nanotechnol. **2019**, *10*, 1401–1411.

doi:10.3762/bjnano.10.138

Received: 04 April 2019

Accepted: 18 June 2019

Published: 15 July 2019

Associate Editor: T. Glatzel

© 2019 Knotek et al.; licensee Beilstein-Institut.

License and terms: see end of document.

Abstract

This study deals with the preparation and characterization of metallic nanoinclusions on the surface of semiconducting Bi₂Se₃ that could be used for an enhancement of the efficiency of thermoelectric materials. We used Au forming a 1D alloy through diffusion (point nanoinclusion) and Mo forming thermodynamically stable layered MoSe₂ nanosheets through the reaction with the Bi₂Se₃. The Schottky barrier formed by the 1D and 2D nanoinclusions was characterized by means of atomic force microscopy (AFM). We used Kelvin probe force microscopy (KPFM) in ambient atmosphere at the nanoscale and compared the results to those of ultraviolet photoelectron spectroscopy (UPS) in UHV at the macroscale. The existence of the Schottky barrier was demonstrated at +120 meV for the Mo layer and –80 meV for the Au layer reflecting the formation of MoSe₂ and Au/Bi₂Se₃ alloy, respectively. The results of both methods (KPFM and UPS) were in good agreement. We revealed that long-time exposure (tens of seconds) to the electrical field leads to deep oxidation and the formation of perturbations greater than 1 μm in height, which hinder the *I*–*V* measurements.

Introduction

Increasing energy demand and the negative effects of current energy technologies on the environment lead to increased interest in alternative energy technologies. Thermoelectric (TE) devices, utilizing TE phenomena, i.e., the Seebeck and the Peltier effect, can be considered solid-state heat engines. The former enables direct waste heat conversion into electrical energy very elegantly (no moving parts, long-term stability, maintenance-free, silent). Unfortunately, one of the limiting factors of this technology is still poor conversion efficiency. The conversion efficiency of the material could be expressed in terms of figure-of-merit, ZT , defined as dimensionless quantity $ZT = S^2 \cdot \sigma \cdot T / \kappa$, where S is the thermopower (Seebeck coefficient), σ is the electrical conductivity, T is the absolute temperature and κ is the thermal conductivity. There were many concepts for enhancement of ZT values, e.g., advanced TE bulk compounds of more complex crystal structures [1], low-dimensional material systems [2] or nanostructured advanced bulk materials [3]. Recently the concept of multi-phase nanocomposites (NCs), i.e., an incorporation of second-phase nanoinclusions/nanoparticles (NIs/NPs) into the bulk semiconducting matrices has been proposed [4-6] and supported in theoretical works [7-9]. Such NIs or NPs are able to enhance ZT via a reduction of the thermal conductivity by phonon scattering [10-14], by modulated carrier doping or by the carrier energy filtering effect [15-17]. The potential energy barrier connected with a metallic NP (Schottky barrier) or a multi-phase interface could scatter low-energy electrons more effectively than high-energy electrons [18]. This, in turn, results in an enhancement of the Seebeck coefficient with virtually no harm to other transport parameters.

The characterization of NIs or NPs in TE materials is realized most frequently by the different modes of atomic force microscopy (AFM): i) by comparing the conductivity/resistivity (CAFM) or $I-V$ curves measurement in the direct-contact of the conductive tip and the material [19-21]; ii) by mapping of the different surface contact potential values by Kelvin probe force microscopy (KPFM) in the semicontact mode [19,22-25], or iii) by measuring the differences in thermal conductivity by scanning thermal microscopy (SThM) [19,20,26]. Shape, size, homogeneity of distribution and chemical composition as the basic characteristics are studied by using electron microscopy (SEM+TEM), although there is a high probability that the NPs diffuse into the TE matrix due to the e-beam interaction. Hence, these characterizations are also performed by using scanning tunneling microscopy (STM) [27,28] or by using AFM in the semicontact mode. The latter enables a description not only of the topography (size and shape) but also a detection of the changes in density, stiffness and adhesion of NPs [20,21,24,29,30].

In the present study we demonstrate that the Schottky barrier (surface contact potential) value and the polarity can be controlled by the barrier-forming metal NPs (Au, Mo) and can reflect their different chemical behavior with the Bi_2Se_3 matrix. These metals were selected due to the different interaction with the matrix, as Au can diffuse to the Bi_2Se_3 forming Au/ Bi_2Se_3 alloy and NIs in the shape of a semispherical defect, whereas Mo reacts with the matrix and forms thermodynamically more stable layered MoSe_2 in the shape of nanosheets.

Experimental

Single crystalline Bi_2Se_3 samples were grown by heating stoichiometric mixtures of the pure elements obtained from Sigma-Aldrich, i.e., 5N Bi and 5N Se. The crystal growth was performed by cooling in a horizontal furnace from 1073 K to 823 K at a rate of 6 K per hour. The crystals were then annealed at 823 K for 350 h and quenched in air. This free-melt crystallization (FMC) procedure produces single crystals of 10–20 mm in length, 3–6 mm in width and up to 3 mm in thickness [31]. The surface of freshly cleaved layered Bi_2Se_3 single crystals was used as a substrate. The samples for the AFM measurement, Au nanoparticles (NPs) and thin films of gold or molybdenum, were prepared via DC sputtering in a SEM Coating System (Bio-Rad) in Ar atmosphere ($p \approx 20$ Pa, $I = 18$ mA, $U = 1.4$ kV) from pure metal sheets (Mo 4N, Au 4N). For preparing separated Au nanoparticles under the same sputtering conditions, however, a stainless steel mask (system of $100 \times 500 \mu\text{m}^2$ holes, 200 holes/ cm^2) between the substrate and target had to be used to decrease the plasma intensity.

The topography, phase shift image, Kelvin probe force microscopy and $I-V$ characteristics were measured by the AFM SolverPro M, Nt-MDT (Russia) with a resolution of 512×512 pixels. The HA_NC tips (resonant frequency 140 kHz, force constant 3.5 N/m) were used for measuring the metal layer thickness by the scratch method and phase contrast [30,32], while conductive NSG01/TiN tips (150 kHz, 5.1 N/m) were used for Kelvin probe force measurements and contact CSG-10/Pt tips (22 kHz, 0.11 N/m) for recording $I-V$ characteristics [33,34] for 10 replicas from an identical point without delay; see the corresponding references above for other experimental details. The set-point was stabilized in the range of 40–50% and the scanning frequency of 0.5 Hz was used, if not mentioned otherwise. A separation of the topographical signal and the V_{CPD} (the contact potential difference) measurement was achieved by the modulation of the V_{AC} at a frequency higher than the bandwidth of the topography feedback system. The topography was measured by the oscillation at the first resonance frequency of the AFM tip, and V_{CPD} was measured by the amplitude of the oscillation at the second resonance fre-

quency of the AFM tip [35,36]. It also has to be noted that all measurements were carried out at room temperature.

Photodiffusion of the metal into Bi_2Se_3 was enabled by means of a Ronchi ruling (non-transparent Cr lines on the SiO_2 substrate) with a density of 2000 lines per millimeter (period 500 nm) as a photomask. The material was illuminated with a UV light source LC08 (Hamamatsu) emitting at wavelengths of 310 and 360 nm; total intensity 0.8 W/cm^2 for 60 s [37,38]. The e-beam diffusion was realized by a SEM JEOL JSM 5500-LV in an area of $8 \times 10 \text{ }\mu\text{m}^2$ with an acceleration voltage of 20 kV (which results in a penetration depth of the electrons of $1 \text{ }\mu\text{m}$ into Bi_2Se_3) for a period of maximally 360 s.

The work function (WF) was determined by ultraviolet photoelectron spectroscopy (UPS) using a helium gas discharge source with He I radiation ($h\nu = 21.22 \text{ eV}$). All UPS measurements were performed in an UHV apparatus (ESCA 2SR, Scienta-Omicron) with a base pressure below 1×10^{-9} mbar.

The spectra were calibrated using the Fermi edge of sputter-cleaned Au as reference. During the measurements, a bias of -10 V was applied to the sample in order to cut off secondary electrons generated in the analyzer. The work function of the sample was calculated as $\text{WF} = h\nu E_{\text{cut-off}}$, where $E_{\text{cut-off}}$ was determined from the intersection of the linear extrapolation of the secondary-electron cut-off (SECO) with the background. All samples were sputtered with argon ions using a scanning focused ion beam source in order to remove surface contaminants. A monoatomic argon ion source was utilized with energy of 2 keV , ion current $10 \text{ }\mu\text{A}$, raster area $1 \times 1 \text{ mm}^2$ and sputtering time 30 s.

Results and Discussion

Separated metal nanoparticles on the substrate

In TE materials the NIs applicable for an increase of their profitability/efficiency should be present as 1D materials or 2D layers. The aim of the characterization of the NIs is the proof of

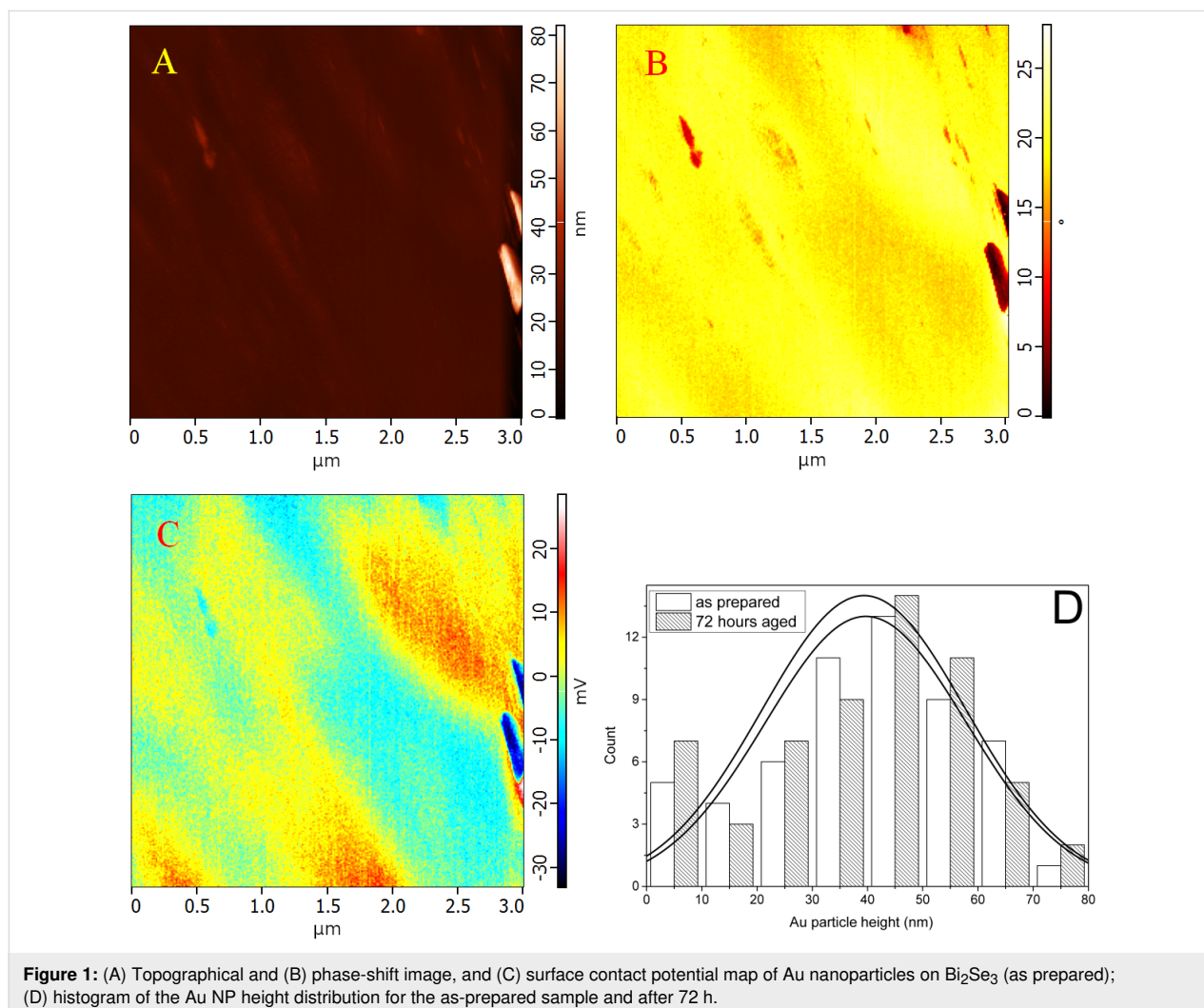


Figure 1: (A) Topographical and (B) phase-shift image, and (C) surface contact potential map of Au nanoparticles on Bi_2Se_3 (as prepared); (D) histogram of the Au NP height distribution for the as-prepared sample and after 72 h.

their presence, the description of their shape and of their electrical behavior in contrast to the unaffected matrix material. We used Bi_2Se_3 as a standard material because of its well-defined layered structure with sub-nanometer roughness similar to mica or highly oriented pyrolytic graphite (HOPG). The electrical conductivity and mechanical stiffness of Bi_2Se_3 allow for the measurement with high-intensity electrical fields (10 V/30 nm) without damaging the topmost layer.

The Au particles were dc-sputtered onto the Bi_2Se_3 substrate and the surface was immediately measured by means of AFM. The particles exhibited a height ranging from 5 to 70 nm. The height distribution (with the maximal population at ca. 40 nm) and the FWHM did not change within 72 h after preparation (Figure 1A and Figure 1D). The stability of the histograms over 3 days led us to believe that during this time interval there is only negligible diffusion of the Au NPs into the Bi_2Se_3 substrate. The material of the particles was mechanically different as observed on the phase shift image (Figure 1B) due to local changes in adhesion, density, and stiffness [30]. This fact demonstrates the difference between the NPs and the substrate, regardless of any artifacts of the sample preparation/measurement.

KPFM is a double-pass measurement technique, where the lift height between the first (topographical) and second (electrical) pass is an important parameter for the spatial resolution [36,39,40]. The tested lift heights were 10, 30 and 50 nm, and the optimal value was found to be 30 nm (Figure 1C). The KPFM image has a good contrast for a lift height of 30 nm and particles with a height less than 10 nm were detected in the map of the surface contact potential. A higher lift height led to a vanishing of the contrast and a lower value resulted in a decrease in reproducibility (data not shown). The results are in a good

agreement with the KPFM contrast of nanodiamonds on a Si substrate, where the contrast even changed for the lower lift height (see Figure 10.2 in [41]). The atypical conductive TiN coating of the tip (instead of Pt, Au Pt/Ir or Pt/Cr tips [33,41–43]) was used because of the higher mechanical stability of the tips and in order to eliminate diffusion and other chemical interactions of the tip coating with the samples. The measured difference of the surface contact potential (Figure 1C) between Au particles and Bi_2Se_3 was not identical for all particles depended on the height of the particles. The height, i.e., the vertical distance between the top of the NP and the substrate and the contrast of the surface contact potential of Au particles (Figure 2A, B) were measured within the same line profile. Au NPs of greater height showed lower values of the surface contact potential according to the non-linear curve limited to a Δ surface contact potential between -50 and -60 mV. This observation can be attributed to quantum size effects [36,44], which are accompanied by a change in the charge transfer from substrate to NPs [45,46].

Metal layers on Bi_2Se_3

The dependence of the surface contact potential on the size of the separated Au nanoparticles theoretically allows for an optimization of the efficiency of TE materials. Our efforts to prepare separated Mo NPs on the Bi_2Se_3 surface was not successful. Because Mo has significantly higher melting/boiling points (bulk Mo 2623/4639 °C, bulk Au 1064/2856 °C [47]) dc sputtering yielded homogeneous layers of Mo instead of separated NPs. In addition, the preparation from colloidal metallic NPs failed as the solvents or stabilizing agents as polyphosphates or vinylpyrrolidones [48] interacted with the uppermost Bi_2Se_3 layer, or residua of the organic solvents that were not evaporated under the vacuum changed the electrical behavior of the nanocomposite.

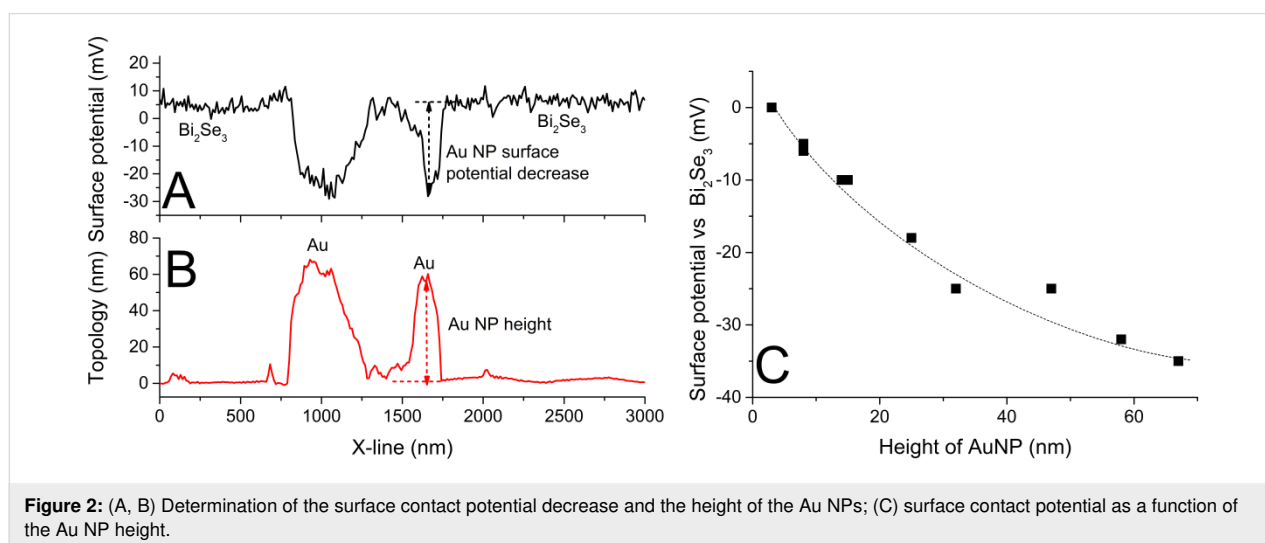


Figure 2: (A, B) Determination of the surface contact potential decrease and the height of the Au NPs; (C) surface contact potential as a function of the Au NP height.

An alternative way to study Schottky barriers at the nanoscale is to prepare a metallic layer on the Bi_2Se_3 surface and characterize such a nanocomposite. I - V spectroscopy is typically used for the determination of Schottky barriers [25,49,50]. The setup was tested on bulk Au and on a 107 nm Au layer on the Bi_2Se_3 (for both cases the contact electrode and conductive tip were located on the same material). We observed a higher conductivity of the bulk material (quantum size effect) (Figure 3, compare curves a) and b)) and a small photodiode effect of Au/ Bi_2Se_3 (-100 mV) due to the AFM illumination (Figure 3, see the intersection of curve b with the x -axis). We also measured Au layers with a thickness of 53 nm and 19 nm (before and after e-beam forced diffusion), and bare Bi_2Se_3 (contact placed on the 107 nm Au layer), see Figure S1, Supporting Information File 1. The curves for each Au thickness at the same area with

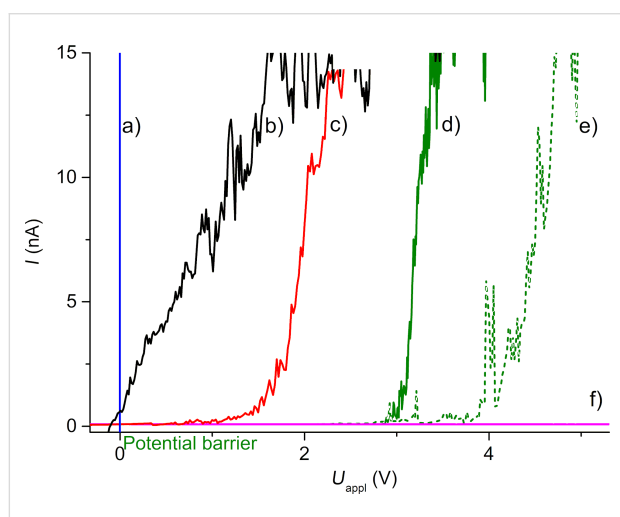


Figure 3: Single-point I - V curves performed during the mechanical contact with the Pt-coated conductive tip on a) bulk Au; b) 107 nm Au layer (both contacts on the same layer); c) 53 nm Au layer; d) and e) 19 nm Au layer before and after e-beam diffusion; f) cleaved Bi_2Se_3 . Curves c-f) were measured with the ohmic contact on the 107 nm Au layer (see Figure S1, Supporting Information File 1).

the best reproducibility are shown in Figure 3. The potential cut-in barrier strongly depends on the Au thickness with values of 1.5 V for the 53 nm Au layer and 3.0 V for 19 nm Au (see Figure 3; curves c, d)). No potential barrier was measurable on Bi_2Se_3 up to 6 V.

There is a systematic increase in the potential cut-in barrier for 53 nm Au/ Bi_2Se_3 upon cycling (Figure 4A). The cut-in barrier was less than 1 V during the first measurement, and above 6 V for the tenth measurement at the same place. The topography also changed significantly after 10 cycles of I - V measurements. Newly formed perturbations were observed with a height of over 1 μm and a FWHM of 2 μm (Figure 4B). The changes in the electrical behavior as well as the growth of the perturbations can be explained by the growth of an isolating oxide layer by anodic oxidation. This has also been observed for Si [51,52], Ti, Ni or Al [53-55], carbon [56] and organic-inorganic compounds [57]. We suggest, in our case, that OH^- or O^-/O_2^- ions diffuse through our polycrystalline Au layer with many defects (grain boundaries, dislocations) forced by the strong electric field (8 V/53 nm of Au, i.e., ca. 1.5×10^8 V/m) [35,36]. At the Au- Bi_2Se_3 interface the oxidation of Bi_2Se_3 can occur accompanied by the formation of non-conductive bismuth oxides (optical $E_g = 3.31$ eV for a 60 nm BiO_x film [58]). Typically, the thickness of surface oxide layers is much lower (of the order of nanometers for SiO_2 on Si [51,52]). In our case it is increased by the electric field and good oxygen mobility in BiO_x due to the formation of charged Bi vacancies [59,60].

This assumption is in good agreement with the observed increase of the cut-in potential barrier upon thinning of the Au layer (see Figure 3) as a reminiscence of the diffusion limitation of oxygen/hydroxy anions due to the electric field through the polycrystalline Au layer. Bare Bi_2Se_3 had no diffusion limits and the I - V curves are not measurable as electrons immediately form isolating BiO_x on the surface. The abovementioned

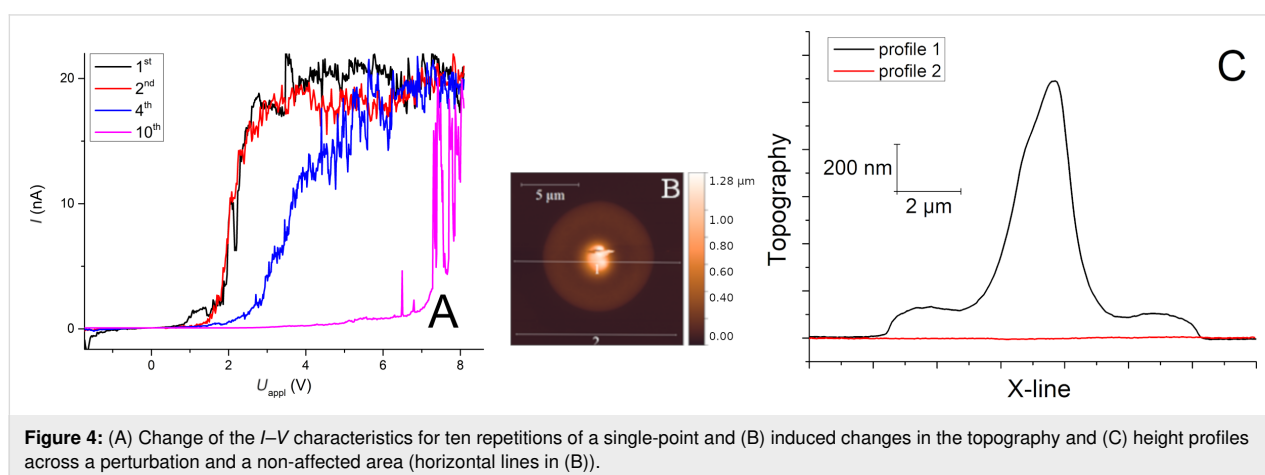


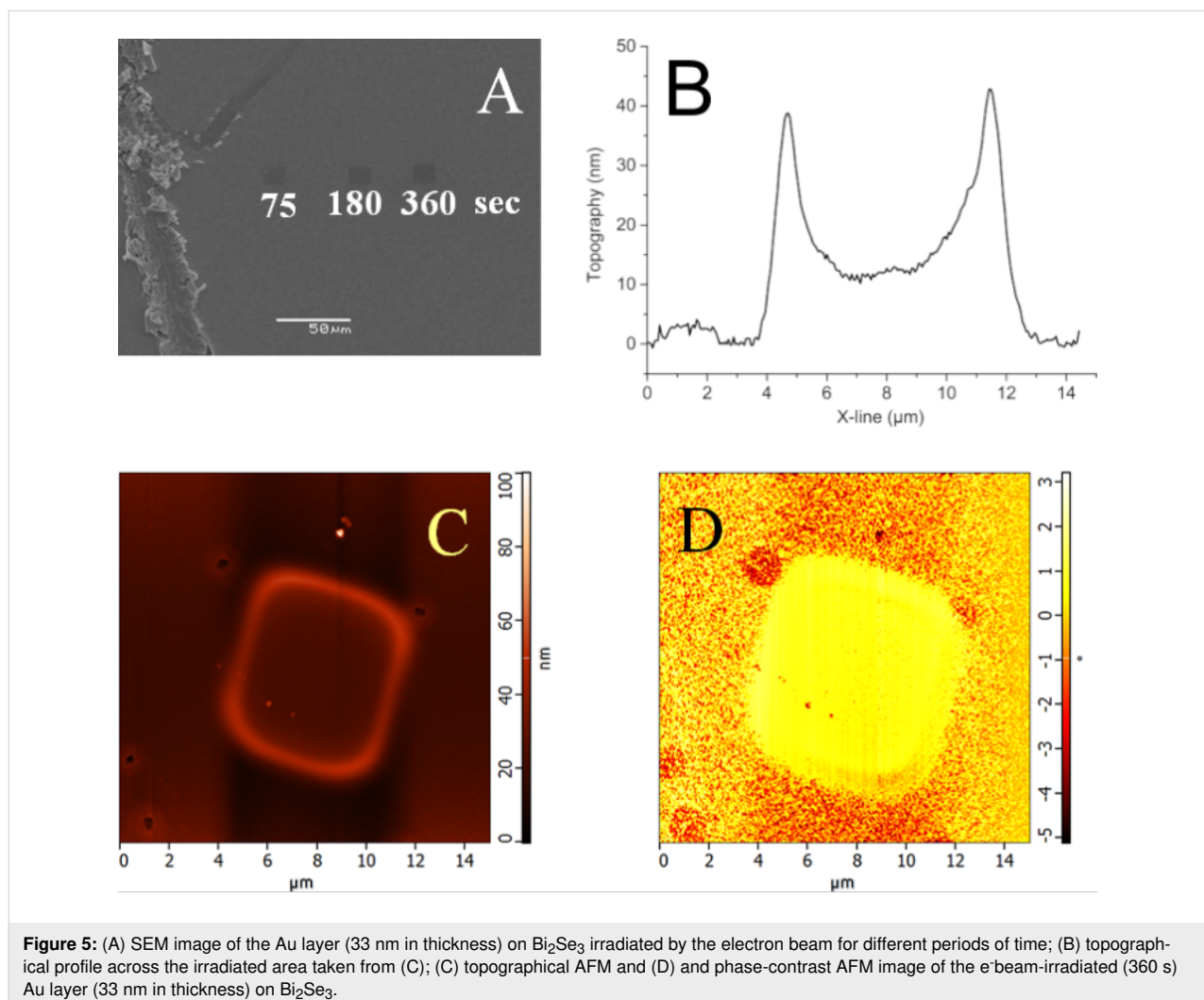
Figure 4: (A) Change of the I - V characteristics for ten repetitions of a single-point and (B) induced changes in the topography and (C) height profiles across a perturbation and a non-affected area (horizontal lines in B)).

tioned facts, tentatively summarized as I – V characteristics, are strongly affected by the oxidation of Bi_2Se_3 . The perturbation with a height of more than 1 μm could be easily formed by the oxidation of a highly O-mobile material, e.g., BiO_x . This limits the usage of I – V measurements in the static electrical contact of the Schottky barrier in ambient atmosphere to stable materials.

KPFM is an alternative way for mapping the changes in the surface contact potential [19,20,26] and reduces force and time of the tip–sample interaction, which in turn reduces the oxidation of the material. The NIs were embedded by local Au diffusion or the reaction of the Mo layer with the Bi_2Se_3 substrate. To enhance the diffusion/reaction rate, we used e-beam irradiation. An area of the $8 \times 10 \mu\text{m}^2$ was locally irradiated by an electron beam for different periods of time (75 s; 180 s and 360 s). This resulted in a nanocomposite material consisting of the metal layer locally reacted with Bi_2Se_3 support and the original metal layer on the support surface. We were able to compare metallic materials with different thicknesses and determine the highest

contrast in the surface contact potential reducing the problem of the diffused interface.

The e-beam-irradiated area exhibits a different SEM signal due to the changes of the chemical composition (Au diffusing into Bi_2Se_3) and changes in the topography (Figure 5). The same NIs, detected by the AFM (Figure 5), exhibited the topographical features of a few tens of nanometers (10 nm in the center and almost 40 nm at the edges) and changes in the phase contrast, both due to the density decrease of the Au alloy upon reaction with the substrate. All samples were irradiated for a period of 360 s. KPFM demonstrated strong variations of the surface contact potential of NIs (measured in the center of the irradiated area) with respect to the non-irradiated area of the Au layer (Figure 6). It should be noted, that the edges of the irradiated area are topographically elevated and exhibit a decreased surface potential because of the higher electron irradiation dose at the turning points of the e-beam. A higher dose led to a higher local temperature, which implies an increased formation



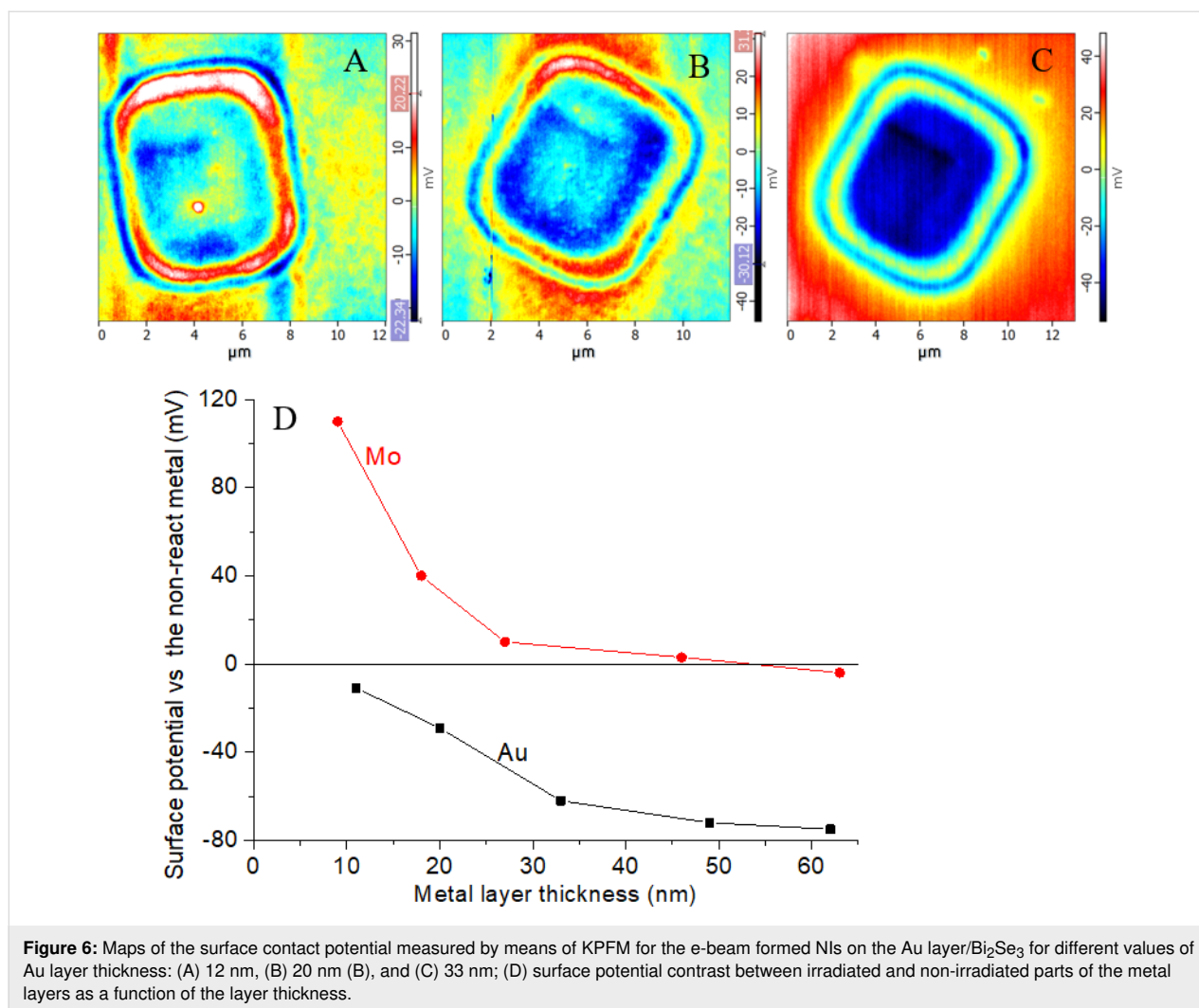


Figure 6: Maps of the surface contact potential measured by means of KPFM for the e-beam formed NIs on the Au layer/ Bi_2Se_3 for different values of Au layer thickness: (A) 12 nm, (B) 20 nm (B), and (C) 33 nm; (D) surface potential contrast between irradiated and non-irradiated parts of the metal layers as a function of the layer thickness.

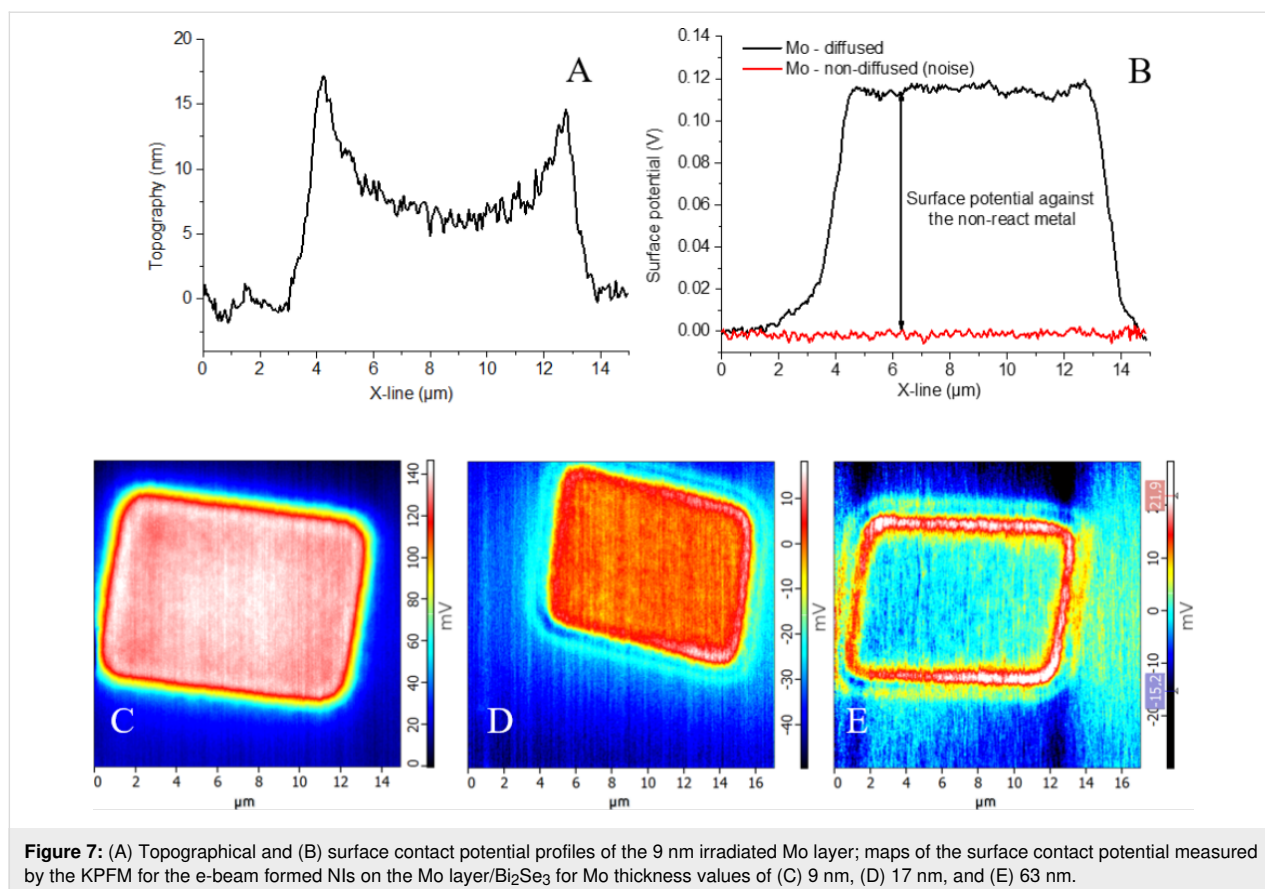
of Au alloy and rims. The comparable so-called “Marangoni effect” was observed in laser-irradiated polymers as described by Lyutakov and co-workers [61].

The NIs formed on the thinnest Au (12 nm) exhibited a surface potential signal slightly above the detection limit of KPFM (Figure 6). With increasing thickness of the Au layer there is a higher contrast (Figure 6). The maximum value of the surface potential difference is between -80 and -90 mV and is connected with the diffusion of Au into Bi_2Se_3 . Although the dependence and the values are alike for 1D particles (Figure 2) and for layers (Figure 6), it is difficult to compare them due to the different “substrate” (Bi_2Se_3 for 1D particles and non-diffused Au for the layers).

The Mo layers on Bi_2Se_3 reacted to the e-beam irradiation in a different way. The irradiated part of the Mo layer expanded less strongly than the Au layer (5 nm at the center, 20 nm at the edge, see Figure 7 profiles) and the contrast in the surface con-

tact potential increased. The most intensive contrast (109 mV) was detected for NIs in the 9 nm thick Mo layer, whereas almost negligible surface contact potential difference (-4 mV) was detected for the 63 nm thick Mo layer.

The results of the surface contact potential mapping at the nano-scale were correlated to the macroscopic work functions (WF) of freshly cleaved Bi_2Se_3 and Au or Mo layers (both 30 nm in thickness). Work functions were measured by surface-sensitive ultraviolet photoelectron spectroscopy (UPS) (Figure 8) employing He I irradiation ($h\nu = 21.22$ eV) with an information depth up to 3 nm. The work function was determined from UPS spectra as an intersection between the background and the linear extrapolation of the secondary-electron cut-off. We obtained $\text{WF}_{\text{Bi}_2\text{Se}_3} = 5.22$ eV, $\text{WF}_{\text{Au}/\text{Bi}_2\text{Se}_3} = 4.79$ eV, $\text{WF}_{\text{Mo}/\text{Bi}_2\text{Se}_3} = 5.98$ eV for Ar^+ -sputtered samples. The WF increased by 760 meV with the Mo layer, whereas the WF decreased by -430 meV after sputtering the Au layer onto Bi_2Se_3 .



We can sum up above results as follows:

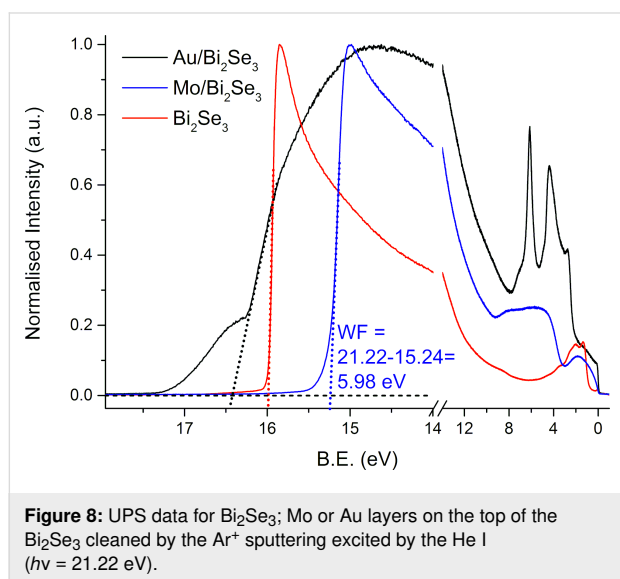
The Au layer on the Bi₂Se₃ surface exhibited lower work function (WF) values than the freshly cleaved Bi₂Se₃ surface, measured by means of the UPS (4.79 eV vs 5.22 eV). This is in good agreement with the decrease of the surface contact potential of the separated Au particles on Bi₂Se₃ detected by the KPFM (limited to -40 mV, see Figure 2C).

The local irradiation of the Au layer on Bi₂Se₃ (Ar⁺ ions before UPS or SEM electrons during formation of NIs for KPFM measurements) led to a reaction with a substrate, most likely the incorporation of interstitial Au atoms into the Bi₂Se₃ matrix and Au alloy/compound formation. This material displayed lower density (topographical expansion, Figure 5) and the creation of the defect states (tentatively connected to the shoulder of the UPS edge, see Figure 8, black curve near 17 eV as well as a decrease in the surface contact potential of the Au NIs, see Figure 6).

In the case of Mo the situation is more complex. We were not able to prepare separated Mo 1D particles due to the higher melting temperature of Mo compared to the Au. The thinnest Mo layer led to the highest contrast in the surface contact poten-

tial of the NIs (see Figure 7) due to the formation of a thermodynamically more stable MoSe₂ layer. The increase in Mo layer thickness led to the presence of the metallic Mo, which is not stable in air and is oxidized within 1 h at RT [62]. The presence of the MoO_x layer is reflected by the high value of the WF (5.98 eV in this work, Mo 4.3 eV and MoSe₂ 5.65 eV as reported in [63]), which fits better to MoO_x layer after the thermal evaporation (6.8 eV) and after 1 h oxidation at air at RT (5.6 eV). Partly oxygen-depleted MoO_x exhibited a WF of 6.36 eV [62]. In our case, non-reacted Mo on the stable MoSe₂ remains reactive (layered MoSe₂ forms a barrier for further Mo diffusion) and Mo reacts with oxygen to produce MoO_x. The UPS information is obtained from the topmost 2–3 nm, i.e., from the oxidized MoO_x layer (30 nm of Mo was sputtered on the Bi₂Se₃ for UPS measurements). The 9 nm Mo layer after SEM electron irradiation led to the formation of MoSe₂ (through the reduction of MoO_x in vacuum to Mo and subsequent reaction with Bi₂Se₃) and these NIs revealed the highest contrast in contact potential (Figure 7). When the thickness of the Mo layer (17 and 63 nm, see Figure 7) is increased, not all Mo reacts to MoSe₂ and there is a cover layer of MoO_x. If the MoO_x layer is irradiated by electrons under the same conditions as the thinnest Mo layer, there will be a partial oxygen depletion as well [62]. However, the long distance from the

Bi_2Se_3 substrate hinders a reaction (the sample exhibits a sandwich structure of reactive Bi_2Se_3 /isolating MoSe_2 /isolating Mo and MoO_x /reactive oxygen-depleted MoO_x). This is further reflected in a low contrast in KPFM measurements, as only non-irradiated and re-oxidized (due to ambient atmosphere) MoO_x layers are measured. Even if MoSe_2 is formed at the MoO_x / Bi_2Se_3 interface, its presence is hidden for both UPS (low information depth) and KPFM (electrons prefer a more conductive path in the Mo/ MoO_x layer).



The applicability of the partial diffusion of the Au layers was tested by the photodiffusion of the 20 nm Au layer into Bi_2Se_3 by UV source through a Ronchi ruling [64,65]. The illuminated Au– Bi_2Se_3 exhibited a periodical pattern of the surface potential with an amplitude of 20 mV (Figure 9). This value is slightly lower in contrast to the NIs obtained by e-beam irradiation of the 20 nm Au layer (decrease 29 mV), and could be connected with the partial lateral diffusion of the heat or Au atoms/ions. In this way, the possibility to prepare a material

with patterned surface contact potential at the macroscopic scale was demonstrated.

Conclusion

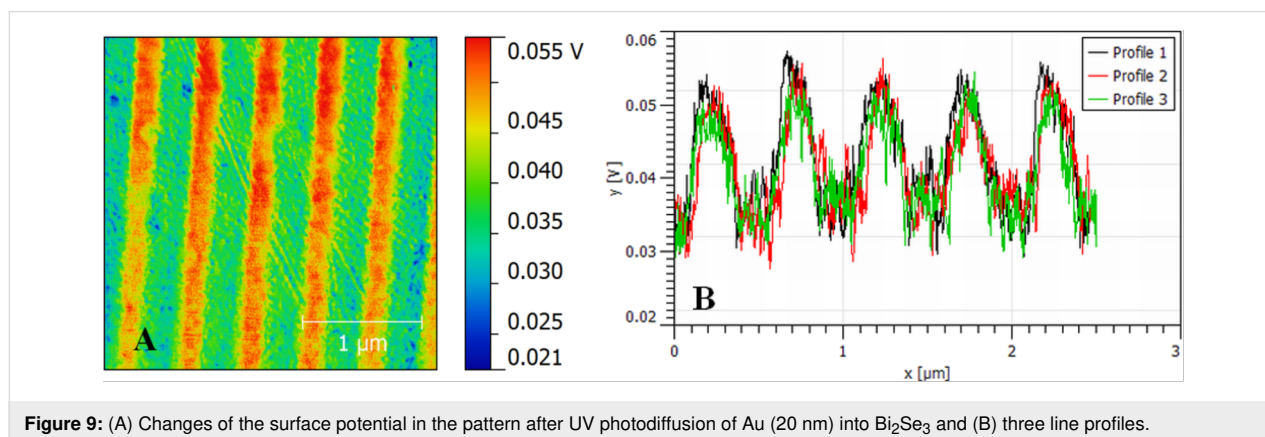
We demonstrated local changes of the work function/surface contact potential as a consequence of metal nanoinclusions on the surface of Bi_2Se_3 . These Schottky barriers can be realized in the form of separated metal nanoparticles through dc sputtering, or through the local reaction/diffusion of a metallic layer irradiated with electrons or UV photons. The value of the work function barrier is measurable by KPFM at the nanoscale even in ambient atmosphere and, most importantly, it strongly depends on the size of the metal particles. The results are in good agreement with the macroscopic UPS results (1 mm^2) obtained in UHV. The investigation of the Schottky barrier in ambient atmosphere is limited to noble metals only, as the Mo nanolayer reacts with oxygen forming MoO_x at RT within a few hours. We therefore conclude that KPFM has the following limitations: i) Only oxidation-resistant metals/semiconductor nanoinclusions can be used. Transition metals react with air and, thus, vacuum equipment is required for the preparation, transport and measurement. ii) The conductive AFM tip has to be coated with a mechanically hard and non-reacting layer as TiN. Typical Au or Pt coatings need to be avoided because the coating might diffuse into the material forced by the electric field during the interaction. iii) The I – V characteristics can be affected by oxidation and perturbations with a height above $1 \mu\text{m}$ can be easily formed by oxidation of a highly O-mobile material such as BiO_x .

Supporting Information

Supporting Information File 1

Scheme of electric circuit.

[<https://www.beilstein-journals.org/bjnano/content/supplementary/2190-4286-10-138-S1.pdf>]



Acknowledgements

The financial support from the Grant Agency of the Czech Republic (GA CR), projects No. 16-07711S and No. 19-11814S is greatly appreciated. The work was supported from European Regional Development Fund-Project "Modernization and upgrade of the CEMNAT (No. CZ.02.1.01/0.0/0.0/16_013/0001829)".

ORCID® iDs

Petr Knotek - <https://orcid.org/0000-0003-2407-4947>

Tomáš Plecháček - <https://orcid.org/0000-0002-9972-4177>

Jan Smolík - <https://orcid.org/0000-0002-4897-2453>

Filip Dvořák - <https://orcid.org/0000-0003-1466-6121>

Čestmír Drašar - <https://orcid.org/0000-0002-5645-5683>

References

- Slack, G. A. *CRC Handbook of Thermoelectrics*; CRC Press: Boca Raton, FL, U.S.A., 1995; p 407.
- Hicks, L. D.; Dresselhaus, M. S. *Phys. Rev. B* **1993**, *47*, 12727–12731. doi:10.1103/physrevb.47.12727
- Liu, W.; Yan, X.; Chen, G.; Ren, Z. *Nano Energy* **2012**, *1*, 42–56. doi:10.1016/j.nanoen.2011.10.001
- Li, H.; Tang, X.; Zhang, Q.; Uher, C. *Appl. Phys. Lett.* **2009**, *94*, 102114. doi:10.1063/1.3099804
- Han, M.-K.; Ahn, K.; Kim, H.; Rhyee, J.-S.; Kim, S.-J. *J. Mater. Chem.* **2011**, *21*, 11365–11370. doi:10.1039/c1jm10163c
- Liu, D.-W.; Li, J.-F.; Chen, C.; Zhang, B.-P. *J. Electron. Mater.* **2011**, *40*, 992–998. doi:10.1007/s11664-010-1476-x
- Faleev, S. V.; Léonard, F. *Phys. Rev. B* **2008**, *77*, 214304–214312. doi:10.1103/physrevb.77.214304
- Zebarjadi, M.; Estarjani, K.; Shakouri, A.; Bahk, J. H.; Bian, Z. X.; Zeng, G.; Bowers, J.; Lu, H.; Zide, J.; Gossard, A. *Appl. Phys. Lett.* **2009**, *94*, 202105. doi:10.1063/1.3132057
- Narducci, D.; Selezneva, E.; Cerofolini, G.; Frabboni, S.; Ottaviani, G. *J. Solid State Chem.* **2012**, *193*, 19–25. doi:10.1016/j.jssc.2012.03.032
- Kulbachinskii, V. A.; Kytin, V. G.; Popov, M. Y.; Buga, S. G.; Stepanov, P. B.; Blank, V. D. *J. Solid State Chem.* **2012**, *193*, 64–70. doi:10.1016/j.jssc.2012.03.065
- Popov, M.; Buga, S.; Vysikaylo, P.; Stepanov, P.; Skok, V.; Medvedev, V.; Tatyani, E.; Denisov, V.; Kirichenko, A.; Aksenenkov, V.; Blank, V. *Phys. Status Solidi A* **2011**, *208*, 2783–2789. doi:10.1002/pssa.201127075
- Park, D.-H.; Kim, M.-Y.; Oh, T.-S. *Curr. Appl. Phys.* **2011**, *11*, S41–S45. doi:10.1016/j.cap.2011.07.007
- Li, F.; Huang, X.; Sun, Z.; Ding, J.; Jiang, J.; Jiang, W.; Chen, L. *J. Alloys Compd.* **2011**, *509*, 4769–4773. doi:10.1016/j.jallcom.2011.01.155
- Li, J.-F.; Liu, J. *Phys. Status Solidi A* **2006**, *203*, 3768–3773. doi:10.1002/pssa.200622011
- Xiong, Z.; Chen, X.; Huang, X.; Bai, S.; Chen, L. *Acta Mater.* **2010**, *58*, 3995–4002. doi:10.1016/j.actamat.2010.03.025
- Dou, Y. C.; Qin, X. Y.; Li, D.; Li, L. L.; Zou, T. H.; Wang, Q. Q. *J. Appl. Phys.* **2013**, *114*, 044906. doi:10.1063/1.4817074
- Zou, T. H.; Qin, X. Y.; Li, D.; Ren, B. J.; Sun, G. L.; Dou, Y. C.; Li, Y. Y.; Li, L. L.; Zhang, J.; Xin, H. X. *J. Appl. Phys.* **2014**, *115*, 053710. doi:10.1063/1.4864220
- Ko, D.-K.; Kang, Y.; Murray, C. B. *Nano Lett.* **2011**, *11*, 2841–2844. doi:10.1021/nl2012246
- Agarwal, K.; Kaushik, V.; Varandani, D.; Dhar, A.; Mehta, B. R. *J. Alloys Compd.* **2016**, *681*, 394–401. doi:10.1016/j.jallcom.2016.04.161
- Agarwal, K.; Mehta, B. R. *J. Appl. Phys.* **2014**, *116*, 083518. doi:10.1063/1.4894145
- Singh, B.; Mehta, B. R.; Varandani, D.; Govind; Narita, A.; Feng, X.; Müllen, K. *J. Appl. Phys.* **2013**, *113*, 203706. doi:10.1063/1.4807411
- Miwa, K.; Salleh, F.; Ikeda, H. *Makara J. Technol.* **2013**, *17*, 17–20. doi:10.7454/mst.v17i1.1922
- Muñoz-Rojo, M.; Caballero-Calero, O.; Martín-González, M. *Appl. Phys. Lett.* **2013**, *103*, 183905. doi:10.1063/1.4826684
- Olaya, D.; Hurtado-Morales, M.; Gómez, D.; Castañeda-Urbe, O. A.; Juang, Z.-Y.; Hernández, Y. *2D Mater.* **2017**, *5*, 011004. doi:10.1088/2053-1583/aa90d8
- Durcan, C. A.; Balsano, R.; LaBella, V. P. *J. Appl. Phys.* **2014**, *116*, 023705. doi:10.1063/1.4889851
- Vanis, J.; Zelinka, J.; Zeipl, R.; Jelinek, M.; Kocourek, T.; Remsa, J.; Navratil, J. *J. Electron. Mater.* **2016**, *45*, 1734–1739. doi:10.1007/s11664-015-4193-7
- Klimovskikh, I. I.; Sostina, D.; Petukhov, A.; Rybkin, A. G.; Ereemeev, S. V.; Chulkov, E. V.; Tereshchenko, O. E.; Kokh, K. A.; Shikin, A. M. *Sci. Rep.* **2017**, *7*, 45797. doi:10.1038/srep45797
- Yamasaka, S.; Nakamura, Y.; Ueda, T.; Takeuchi, S.; Sakai, A. *Sci. Rep.* **2015**, *5*, 14490. doi:10.1038/srep14490
- Bala, M.; Gupta, S.; Tripathi, T. S.; Varma, S.; Tripathi, S. K.; Asokan, K.; Avasthi, D. K. *RSC Adv.* **2015**, *5*, 25887–25895. doi:10.1039/c5ra01000d
- Knotek, P.; Chanova, E.; Rypacek, F. *Mater. Sci. Eng., C* **2013**, *33*, 1963–1968. doi:10.1016/j.msec.2013.01.006
- Cermak, P.; Ruleova, P.; Holy, V.; Prokleska, J.; Kucek, V.; Palka, K.; Benes, L.; Drasar, C. *J. Solid State Chem.* **2018**, *258*, 768–775. doi:10.1016/j.jssc.2017.12.009
- Knotek, P.; Tichý, L. *Thin Solid Films* **2009**, *517*, 1837–1840. doi:10.1016/j.tsf.2008.09.041
- Knotek, P.; Tasseva, J.; Petkov, K.; Kincl, M.; Tichy, L. *Thin Solid Films* **2009**, *517*, 5943–5947. doi:10.1016/j.tsf.2009.04.038
- Das, S.; Zazpe, R.; Prikryl, J.; Knotek, P.; Krbal, M.; Sopha, H.; Podzemna, V.; Macak, J. M. *Electrochim. Acta* **2016**, *213*, 452–459. doi:10.1016/j.electacta.2016.07.135
- Glatzel, T.; Sadewasser, S.; Lux-Steiner, M. C. *Appl. Surf. Sci.* **2003**, *210*, 84–89. doi:10.1016/s0169-4332(02)01484-8
- Melitz, W.; Shen, J.; Kummel, A. C.; Lee, S. *Surf. Sci. Rep.* **2011**, *66*, 1–27. doi:10.1016/j.surfrep.2010.10.001
- Knotek, P.; Tichy, L.; Kutalek, P. *Thin Solid Films* **2015**, *594*, 67–73. doi:10.1016/j.tsf.2015.09.055
- Knotek, P.; Vleck, M.; Kincl, M.; Tichy, L. *Thin Solid Films* **2012**, *520*, 5472–5478. doi:10.1016/j.tsf.2012.03.116
- Axt, A.; Hermes, I. M.; Bergmann, V. W.; Tausendpfund, N.; Weber, S. A. L. *Beilstein J. Nanotechnol.* **2018**, *9*, 1809–1819. doi:10.3762/bjnano.9.172
- Sadewasser, S.; Nicoara, N.; Solares, S. D. *Beilstein J. Nanotechnol.* **2018**, *9*, 1272–1281. doi:10.3762/bjnano.9.119
- Rezek, B.; Stehlik, S. Chapter 10 - Surface potential of nanodiamonds investigated by KPFM. In *Nanodiamonds*; Arnault, J.-C., Ed.; Elsevier: Amsterdam, Netherlands, 2017; pp 273–300. doi:10.1016/b978-0-32-343029-6.00011-8
- Watanabe, T.; Fujihira, M. *Ultramicroscopy* **2009**, *109*, 1035–1039. doi:10.1016/j.ultramic.2009.03.047

43. Zeng, T.-W.; Hsu, F.-C.; Tu, Y.-C.; Lin, T.-H.; Su, W.-F. *Chem. Phys. Lett.* **2009**, *479*, 105–108. doi:10.1016/j.cplett.2009.07.104
44. Yamauchi, T.; Tabuchi, M.; Nakamura, A. *Appl. Phys. Lett.* **2004**, *84*, 3834–3836. doi:10.1063/1.1745110
45. Sasahara, A.; Pang, C. L.; Onishi, H. *J. Phys. Chem. B* **2006**, *110*, 17584–17588. doi:10.1021/jp063665h
46. Sasahara, A.; Hiehata, K.; Onishi, H. *Catal. Surv. Asia* **2009**, *13*, 9–15. doi:10.1007/s10563-009-9062-z
47. Lide, D. R. *Handbook of Chemistry and Physics*, 84th ed.; CRC Press: Boca Raton, FL, U.S.A., 2003.
48. *Nanomaterials: Synthesis, Properties and Applications*; J. W. Arrowsmith, Ltd.: Bristol, United Kingdom, 1996.
49. Lee, H.; Keun Lee, Y.; Nghia Van, T.; Young Park, J. *Appl. Phys. Lett.* **2013**, *103*, 173103. doi:10.1063/1.4826140
50. Tedesco, J. L.; Rowe, J. E.; Nemanich, R. J. *J. Appl. Phys.* **2009**, *105*, 083721. doi:10.1063/1.3100212
51. Avouris, P.; Martel, R.; Hertel, T.; Sandstrom, R. *Appl. Phys. A: Mater. Sci. Process.* **1998**, *66*, S659–S667. doi:10.1007/s003390051218
52. Tello, M.; Garcia, R. *Appl. Phys. Lett.* **2001**, *79*, 424–426. doi:10.1063/1.1385582
53. Irmer, B.; Kehrlé, M.; Lorenz, H.; Kotthaus, J. P. *Appl. Phys. Lett.* **1997**, *71*, 1733–1735. doi:10.1063/1.120019
54. Fang, T.-H.; Chen, K.-J. *Mater. Trans.* **2007**, *48*, 471–475. doi:10.2320/matertrans.48.471
55. Shingubara, S.; Murakami, Y.; Morimoto, K.; Takahagi, T. *Surf. Sci.* **2003**, *532–535*, 317–323. doi:10.1016/s0039-6028(03)00433-3
56. Chuang, M.-C.; Chien, H.-M.; Chain, Y.-H.; Chi, G.-C.; Lee, S.-W.; Woon, W. Y. *Carbon* **2013**, *54*, 336–342. doi:10.1016/j.carbon.2012.11.045
57. Baumgärtel, T.; von Borczyskowski, C.; Graaf, H. *Beilstein J. Nanotechnol.* **2013**, *4*, 218–226. doi:10.3762/bjnano.4.22
58. Leontie, L.; Caraman, M.; Alexe, M.; Harnagea, C. *Surf. Sci.* **2002**, *507–510*, 480–485. doi:10.1016/s0039-6028(02)01289-x
59. Zhong, G.; Wang, Y.; Dai, Z.; Wang, J.; Zeng, Z. *Phys. Status Solidi B* **2009**, *246*, 97–101. doi:10.1002/pssb.200844271
60. Torruella, P.; Coll, C.; Martín, G.; López-Conesa, L.; Vila, M.; Díaz-Guerra, C.; Varela, M.; Ruiz-González, M. L.; Piqueras, J.; Peiró, F.; Estradé, S. *J. Phys. Chem. C* **2017**, *121*, 24809–24815. doi:10.1021/acs.jpcc.7b06310
61. Lyutakov, O.; Huttel, I.; Siegel, J.; Švorčík, V. *Appl. Phys. Lett.* **2009**, *95*, 173103. doi:10.1063/1.3254210
62. Irfan, I.; James Turinske, A.; Bao, Z.; Gao, Y. *Appl. Phys. Lett.* **2012**, *101*, 093305. doi:10.1063/1.4748978
63. Keszler, D. A.; Wager, J. F. *Novel Materials Development for Polycrystalline Thin-Film Solar Cells: Final Subcontract Report, 26 July 2004--15 June 2008*; Office of Scientific and Technical Information (OSTI), 2008; pp 1–16. doi:10.2172/942065
64. Balakrishnan, M.; Kozicki, M. N.; Poweleit, C. D.; Bhagat, S.; Alford, T. L.; Mitkova, M. *J. Non-Cryst. Solids* **2007**, *353*, 1454–1459. doi:10.1016/j.jnoncrysol.2006.09.071
65. Adam, J.-L.; Zhang, X., Eds. *Woodhead Publishing Series in Electronic and Optical Materials*; Elsevier: Amsterdam, Netherlands, 2014.

License and Terms

This is an Open Access article under the terms of the Creative Commons Attribution License (<http://creativecommons.org/licenses/by/4.0>). Please note that the reuse, redistribution and reproduction in particular requires that the authors and source are credited.

The license is subject to the *Beilstein Journal of Nanotechnology* terms and conditions: (<https://www.beilstein-journals.org/bjnano>)

The definitive version of this article is the electronic one which can be found at: doi:10.3762/bjnano.10.138